

















RESEARCH ARTICLE

10.1029/2022JA030527

Pronounced Suppression and X-Pattern Merging of Equatorial Ionization Anomalies After the 2022 Tonga Volcano Eruption

Key Points:

- Daytime equatorial ionization anomaly (EIA) crests eroded severely by 10+ TEC Unit and collapsed equatorward over 10° latitude, following the arrival of volcano-induced Lamb waves
- EIA crests exhibited a unique deformation after sunset with an X-pattern merging in a longitudinally confined area between 20° and 40°W
- Thermospheric zonal wind showed post-volcanic oscillations of ±200 m/s that may explain the EIA suppression and X-pattern via dynamo effect

Ercha Aa¹ , Shun-Rong Zhang¹ , Wenbin Wang² , Philip J. Erickson¹ , Liying Qian² , Richard Eastes³ , Brian J. Harding⁴ , Thomas J. Immel⁴, Deepak K. Karan³ , Robert E. Daniell⁵ , Anthea J. Coster¹ , Larisa P. Goncharenko¹ , Juha Vierinen⁶ , Xuguang Cai³ , and Andres Spicher⁶ 

¹Haystack Observatory, Massachusetts Institute of Technology, Westford, MA, USA, ²High Altitude Observatory, National Center for Atmospheric Research, Boulder, CO, USA, ³Laboratory for Atmospheric and Space Physics, University of Colorado, Boulder, CO, USA, ⁴Space Sciences Laboratory, University of California, Berkeley, CA, USA, ⁵Ionospheric Physics, Stoughton, MA, USA, ⁶Department of Physics and Technology, The Arctic University of Norway, Tromsø, Norway

Correspondence to:

E. Aa,
aercha@mit.edu

Citation:

Aa, E., Zhang, S.-R., Wang, W., Erickson, P. J., Qian, L., Eastes, R., et al. (2022). Pronounced suppression and X-pattern merging of equatorial ionization anomalies after the 2022 Tonga volcano eruption. *Journal of Geophysical Research: Space Physics*, 127, e2022JA030527. <https://doi.org/10.1029/2022JA030527>

Received 5 APR 2022
Accepted 25 MAY 2022

Abstract Following the 2022 Tonga Volcano eruption, dramatic suppression and deformation of the equatorial ionization anomaly (EIA) crests occurred in the American sector ~14,000 km away from the epicenter. The EIA crests variations and associated ionosphere-thermosphere disturbances were investigated using Global Navigation Satellite System total electron content data, Global-scale Observations of the Limb and Disk ultraviolet images, Ionospheric Connection Explorer wind data, and ionosonde observations. The main results are as follows: (a) Following the eastward passage of expected eruption-induced atmospheric disturbances, daytime EIA crests, especially the southern one, showed severe suppression of more than 10 TEC Unit and collapsed equatorward over 10° latitudes, forming a single band of enhanced density near the geomagnetic equator around 14–17 UT, (b) Evening EIA crests experienced a drastic deformation around 22 UT, forming a unique X-pattern in a limited longitudinal area between 20 and 40°W. (c) Thermospheric horizontal winds, especially the zonal winds, showed long-lasting quasi-periodic fluctuations between ±200 m/s for 7–8 hr after the passage of volcano-induced Lamb waves. The EIA suppression and X-pattern merging was consistent with a westward equatorial zonal dynamo electric field induced by the strong zonal wind oscillation with a westward reversal.

Plain Language Summary The extreme Tonga volcano eruption on 15 January 2022 triggered profound and prolonged disturbances in the equatorial ionosphere. Using ground-based Global Navigation Satellite System total electron content and ionosonde data, low-Earth orbiting Ionospheric Connection Explorer wind observations, and geostationary Global-scale Observations of the Limb and Disk ultraviolet measurements of thermospheric and ionospheric airglow emission, we found volcano-induced atmospheric Lamb waves as a plausible source of the observed pronounced deformation of equatorial ionization anomaly (EIA) in the American sector. This deformation was triggered by volcano-induced wave passage through the region, even after these waves had traveled 12,000–16,000 km distance for over 10 hr. The typical double-crested EIA morphology was severely deformed during both the daytime and nighttime. Daytime EIA crests exhibited a severe suppression of more than 10 TEC Unit (TECu) (1TECu = 10¹⁶ m⁻²) and an equatorward collapse around 14–17 UT (10–13 LT) especially for the southern crest. Nighttime EIA crests exhibited a unique X-pattern with crests drastically merging in a narrow longitude region between 20 and 40°W around 22 UT (20 LT). These large EIA deformations were coincident, sharing spatial scales with long-lasting oscillations of thermospheric zonal wind following the arrival of volcano-induced waves in the American sector. This study sheds new light on the potential far-reaching and long-lasting atmosphere-ionosphere-thermosphere impacts from a catastrophic geological event.

1. Introduction

The equatorial ionization anomaly (EIA) is a pronounced phenomenon in the low-latitude ionosphere F-layer with double plasma density crests around ±15° geomagnetic latitudes and an equatorial density trough (Appleton, 1946; Balan et al., 2018; Duncan, 1960). It is generally explained by the “fountain effect” in terms of drift and diffusion: an eastward daytime dynamo electric field around the magnetic equator lifts the ionospheric plasma to higher altitudes via upward $E \times B$ drifts; subsequently, increased gravitational and pressure gradient forces

© 2022 The Authors.

This is an open access article under the terms of the [Creative Commons Attribution-NonCommercial License](https://creativecommons.org/licenses/by/4.0/), which permits use, distribution and reproduction in any medium, provided the original work is properly cited and is not used for commercial purposes.

then lead to a poleward and downward plasma diffusion along magnetic field lines, causing concentrated density crests in the off-equatorial region and a trough near the equator (e.g., Anderson, 1973; Balan & Bailey, 1995; Hanson & Moffett, 1966). EIA morphology and spatiotemporal characteristics, such as local time, longitude, altitude, interhemispheric asymmetry, and solar activity dependence, have been extensively studied using ionosonde observations (e.g., Jayachandran et al., 1997; Thomas, 1968), Global Navigation Satellite System Total Electron Content (GNSS TEC) data (e.g., Das et al., 2014; Wan et al., 2021; Zhao et al., 2009), radio occultation data (e.g., Huang et al., 2018; Lin et al., 2007; Luan et al., 2015; Tulasi Ram et al., 2009), satellite in-situ measurements (e.g., Chen et al., 2016; Paul & Dasgupta, 2010; Xiong et al., 2013), remote sensing measurements (e.g., Basu et al., 2009; Cai et al., 2021, 2020; Eastes et al., 2019; Kil et al., 2006), and numerical simulations (e.g., Dang et al., 2016; Lei et al., 2012; Su et al., 1997).

EIA crests are some of the most dramatic electron density enhancement structures in the global ionosphere, occurring on a regular basis during the day and earlier evening hours. The intensity and position of EIA crests have complicated short-term (hours to a day) spatiotemporal variability that is still not fully understood. Crest properties can be significantly influenced by various electrodynamic, dynamic, and chemical processes such as: (a) *Zonal electric field*: Besides the prevailing daytime E-region dynamo, increased F-region zonal wind and conductivity gradients near sunset develop an enhanced eastward electric field and upward drift around the magnetic equator, known as the prereversal enhancement (PRE) (Eccles et al., 2015; Farley et al., 1986), with this factor driving continued EIA prominence in postsunset hours. Moreover, storm-time penetration electric fields due to varying magnetospheric convection, and the disturbance dynamo electric field caused by changes in global thermosphere circulation, greatly modify the equatorial zonal electric field and significantly impact EIA morphology (e.g., Balan et al., 2009; Sreeja et al., 2009; Tsurutani et al., 2004). (b) *Magnetic meridional winds*: These winds drag the plasma along magnetic field lines and impact the EIA in two opposite ways. First, drag forcing by the equatorward (poleward) wind raises or lowers the F-region height to regions with lower or higher plasma recombination rates, causing a stronger (weaker) EIA crest closer to (away from) the equator (Khadka et al., 2018; Tulasi Ram et al., 2009). Second, trans-equatorial wind can transport the plasma either with or against the background ambipolar diffusion direction, sometimes causing an intensified/weak EIA crest in the winter/summer hemisphere during the morning-time before an afternoon transition occurs (Dang et al., 2016; Huang et al., 2018; Lin et al., 2007). (c) *Neutral composition effect*: High-latitude thermospheric composition (e.g., O/N_2) changes, especially during storm-time periods, are carried by an equatorward wind surge to low-latitudes, causing inhibited EIA crests in the recovery phase (e.g., Aa et al., 2021; Fuller-Rowell et al., 1994; Sreeja et al., 2009). (d) *Large-scale waves from the lower atmosphere*: Tides and planetary waves may cause prominent EIA longitudinal structures (e.g., wave-4) and longer-term (e.g., 6-day or 16-day) quasi-periodic oscillations (e.g., Gan et al., 2020; Goncharenko et al., 2010; Immel et al., 2006; Yamazaki, 2018). However, some modeling studies have suggested that large-scale atmospheric waves can cause strong day-to-day variability in the equatorial ionosphere vertical drift, although more direct observational evidence is needed (Fang et al., 2018; Liu, 2020). The combination of all these processes creates complicated short-term variability of EIA crest features.

Although the neutral wind dynamo which drives EIA dynamics is known to be subject to lower atmospheric forcing, there has been no established direct connection to date between EIA short-term variability and underlying geological events such as earthquakes and volcanic eruptions, let alone any remote connection to such events over thousands of km distance. The present EIA study, however, provides compelling evidence for such a plausible remote connection during an intense volcanic eruption event at Tonga at 04:14:45 UT on 15 January 2022. We assert that the response to such an event points to a new mechanism for efficient vertical coupling between explosive lithospheric disturbances and upper atmospheric changes. Such a connection was possible because of substantial global propagation of eruption-related atmospheric waves such as Lamb waves (e.g., Themens et al., 2022; Zhang et al., 2022) and their huge impact on thermospheric dynamics and therefore ionospheric electrodynamic (Harding et al., 2022). Ionospheric responses, the focus of this study, were characterized by a unique suppression and deformation of EIA crests with an X-shaped spatial pattern (Daniell et al., 2021). The detailed study results are elaborated in the following sections, using ground-based GNSS TEC data, ionosonde measurements, Global-scale Observations of the Limb and Disk (GOLD) imager data, and Ionospheric Connection Explorer (ICON) wind measurements.

2. Instruments and Data Description

GNSS TEC data are derived at Massachusetts Institute of Technology's Haystack Observatory utilizing 5,000+ worldwide ground-based GNSS receivers, which are provided to the community via the Madrigal distributed data system with a spatial resolution of 1° (longitude) \times 1° (latitude) and a temporal cadence of 5 min (Rideout & Coster, 2006; Vierinen et al., 2016). Besides ground-based GNSS TEC, South American sector ionosonde measurements at Fortaleza (3.9°S, 38.4°W) are also utilized.

The GOLD instrument images the Earth's ionosphere and thermosphere from a geostationary orbit at 47.5°W, using two identical ultraviolet imaging spectrometers to measure Earth's airglow emissions between 134 and 160 nm from a roughly constant pressure surface over the daytime/nighttime disk, limb, and stellar occultation (Eastes et al., 2017, 2019). The daytime disk measurements can be used to derive thermospheric temperature and neutral composition ratio. The limb observations are used to retrieve exospheric temperature information as well as molecular oxygen column density from stellar occultations. Nighttime disk measurements are used to derive equatorial and low-latitude ionospheric structures especially the EIA and plasma irregularities. This study uses nighttime disk measurements of atomic oxygen 135.6 nm emissions to show EIA variations, which is mainly produced by recombination reaction between oxygen ions and electron. For more details on GOLD measurements, readers may refer to Eastes et al. (2020) and references therein.

ICON is a low-Earth orbit satellite for ionospheric and thermospheric measurements at an altitude of 575 km and an inclination angle of 27° (Immel et al., 2018). ICON carries the Michelson Interferometer for Global High-Resolution Thermospheric Imaging (MIGHTI) instrument to measure thermospheric wind velocity and temperature with observations on Earth's limb. This study analyzes version 04 thermospheric vector wind data that derived from MIGHTI Doppler shift observations of the 630.0 nm oxygen red line (\sim 160–300 km altitude) and 557.7 nm green line (\sim 90–200 km altitude) airglow emissions. For more information on MIGHTI instrument and observations, readers may refer to Englert et al. (2017), Harding et al. (2017), and Makela et al. (2021).

3. Results

3.1. Interplanetary and Geomagnetic Conditions

Figures 1a–1d show temporal variations of solar wind speed and proton density, interplanetary magnetic field (IMF) B_y and B_z components, planetary K-index (K_p), and the longitudinally symmetric index (SYM-H) between January 13–17, 2022. On January 14, an interplanetary coronal mass ejection (CME) arrived with a sudden increase in solar wind proton density at \sim 13 UT. The IMF B_z rotated to a sustained southward direction after 14:50 UT, reaching a minimum value of -17 nT at 22:25 UT and then quickly flipping northward. Solar wind speeds increased from \sim 340–380 km/s to near 440 km/s. The SYM-H index reached a minimum value of -100 nT at 22:25 UT, marking the peak of the storm main phase with K_p of 6. During the recovery phase on January 15–16, continued disturbances occurred due to recurrent coronal hole high-speed streams. The solar wind speed increased from 450 km/s to 550 km/s at 15 UT on January 15, further increased to 620 km/s at 00:50 UT on January 16, and held steady between 530 and 650 km/s throughout the day. IMF B_z exhibited intermittent fluctuations between ± 7 nT during 18–24 UT on January 15 and smaller perturbations continued on January 16. SYM-H showed a second dip, reaching -53 nT at \sim 01 UT on January 16, with a following gradual recovery. Taken as a whole, the combination of CME and coronal hole high-speed stream effects created a moderate geomagnetic storm before the Tonga volcano eruption at 04:15 UT (red line) on January 15.

3.2. EIA Suppression and X-Pattern Merging

To provide broad synoptic views of EIA, Figures 1e–1h display combined maps of GNSS TEC and OI 135.6 nm radiance from GOLD ultraviolet imaging at 22:10 UT on January 13–16. TEC observations over the American sector show afternoon EIA crests approximately paralleling $\pm 15^\circ$ geomagnetic latitudes. GOLD images over the Atlantic/African sector show bright low-latitude arcs produced by enhanced oxygen ion density and emission, and indicate postsunset EIA crests (Eastes et al., 2019). Note the OI 135.6 nm emission radiance is approximately proportional to the square of peak electron density, which increases the display contrast that makes the nighttime EIA crests look more well-developed comparing with daytime ones.

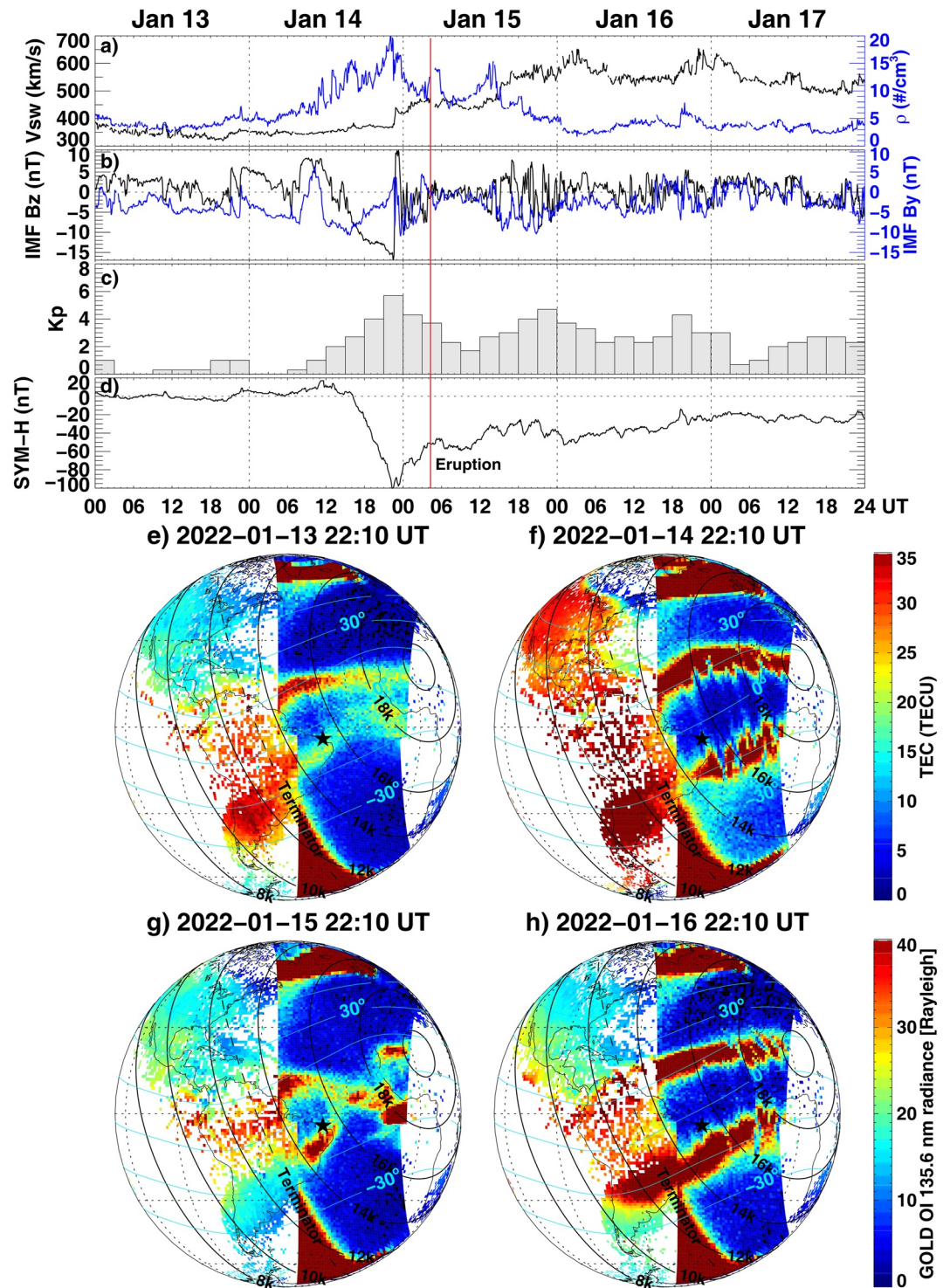


Figure 1. Temporal variation of (a) Solar wind speed and proton density, (b) Interplanetary magnetic field (IMF) B_y and B_z, (c) K_p index, and (d) Longitudinally symmetric index (SYM-H) during January 13–17, 2022. The volcano eruption time is marked with a vertical red line. (e–h) Combined Global Navigation Satellite System total electron content (TEC) and Global-scale Observations of the Limb and Disk (GOLD) OI 135.6-nm radiance maps at 22:10 UT on January 13–16, 2022. The iso-distance circles from the Tonga eruption epicenter are shown in black lines. Geomagnetic latitudes with 15° interval are shown in cyan lines. The Fortaleza ionosonde location is marked with a black star. Note the enhanced GOLD radiance emission in the polar region is due to auroral precipitation. The triangular-shape enhancement at the bottom of GOLD images is due to strong daytime airglow near the terminator under the influence of sunlight.

Large day-to-day EIA variability can be seen in Figures 1e–1h. On the quiet day of January 13, the EIA appeared relatively smooth and the crests location were around $\pm 10\text{--}15^\circ$ geomagnetic latitudes. By comparison, on January 14 during storm main phase, GNSS TEC was significantly enhanced by 10–15 TEC Unit (TECU) ($\sim 50\text{--}100\%$) in the EIA area and the whole sunlit region, due to a strong penetration electric field effect associated with continuous southward IMF Bz conditions during 14:50–22:30 UT. After sunset, GOLD data also showed that EIA crests were considerably intensified and broadened due to the storm-enhanced fountain effect, with crests locations shifted poleward to $\pm 15\text{--}25^\circ$ latitudes. GOLD also captured multiple dark streaks cutting through the equatorward edge of EIA crests, indicating equatorial plasma bubbles due to enhanced Rayleigh-Taylor instability growth rates caused by the presence of PRE and penetration electric fields (e.g., Aa et al., 2020; Eastes et al., 2020; Karan et al., 2020). On January 15, however, the EIA morphology was significantly deformed. In the daytime, the EIA as seen in TEC over South America was significantly suppressed, with two crests pushed toward the dip equator with $<10^\circ$ separation. The EIA intensity, especially the southern crest, was significantly depleted by $\sim 50\%$ compared to January 13 and 14. On the nightside, two EIA crests were still visible in GOLD data. However, they moved toward each other over the Atlantic, merging into one structure at the equator centered at a narrow longitudinal area near 30°W . The EIA then separated into two distinct crests forming a twisted pattern, resembling an “X-pattern” located approximately 16,000–17,000 km away from the volcano eruption epicenter. On January 16, the EIA morphology recovered to typical pattern with two crests being clearly identified and separated. This coincident combination of EIA dayside suppression and nightside X-pattern after volcano eruption has, to the best of our knowledge, never been simultaneously reported before and will be further analyzed here.

To understand the thermosphere-ionosphere drivers of the observed EIA suppression and X-pattern, Figures 2a–2c show the ICON MIGHTI instrument’s observation track and corresponding thermospheric zonal and meridional wind profiles between 20:48–21:16 UT on January 15. The blue circle in Figure 2a marks the estimated wavefront location of volcano-induced Lamb waves at the time of ICON passage through the region. Large horizontal wind changes can be seen in the F region. In addition, significant westward zonal wind reversal of -200 m/s can be observed at the trailing edge of volcano-induced Lamb waves (Figure 2b), around 150–240 km altitude between 15 and 40°W longitudes and 16,000–18,000 km iso-distance lines. However, we note that these nighttime data points below 240 km are likely dominated by noise where the red line signal is dim with large uncertainties.

To trace the X-pattern formation with respect to wind variation, Figures 2d–2i display consecutive GNSS TEC and GOLD nighttime OI 135.6 nm radiance maps showing a sequence of EIA evolution during 20:40–23:55 UT. Observations indicate that from 20:40 UT (Figure 2d) to 21:40 UT (Figure 2f), EIA morphology became severely twisted with the intensity of both crests being considerably suppressed and location severely collapsed toward the dip equator near $20^\circ\text{--}40^\circ\text{W}$. At 22:10 UT (Figure 2g), a clear X-pattern was fully developed with two EIA crests “merging” together around $20^\circ\text{--}40^\circ\text{W}$ but separated on both the eastern and western sides. The location and time of the ionospheric X-pattern formation is consistent with large horizontal wind changes in the F region, suggesting a plausible correlation with westward equatorial zonal electric field due to the dynamo effect that will be further discussed in the following section. Starting from 22:40 UT, the eastern side of X-pattern rotated out of GOLD’s field of view, and dark streaks of postsunset equatorial plasma bubbles (EPBs) were generated and extended along the field lines along the western side of X-pattern.

EIA evolution is also examined in Figures 3a–3d using TEC keograms as a function of time and latitude along 60°W during January 13–16. All observation days except for January 15 showed distinct and typical double-crest features that approximately aligned with $\pm 15^\circ$ geomagnetic latitudes. However, EIA morphology on January 15 (Figure 3c) was significantly different with weaker intensities and two clear X-pattern merging features. The first X-pattern appeared at midday with crests especially the southern one being severely depleted by over 10 TECU and collapsed equatorward by more than 10° from 13 to 14 UT to 16–17 UT (marked by black arrows in Figure 3c), forming one broadband shape near the equator. The second X-pattern occurred near dusktime at 21–23 UT with two crests merged again to form a discernible single equatorial band. This is consistent with the timing of GOLD observations of X-pattern.

The distinct EIA variation and X-pattern signature can also be observed in the longitudinal TEC keogram shown in Figure 3g. A red arrow marks an eastward TEC erosion feature at 14–18 UT propagating from 10,000 km to 14,000 km iso-distance lines. The disturbance propagation velocity was estimated to be 310–330 m/s, consistent with the atmospheric Lamb wave speed described in recent studies (e.g., Themens et al., 2022; Zhang et al., 2022). At the leading (left) side of the wave, TEC exhibited a modest increase parallel to the arrow especially between

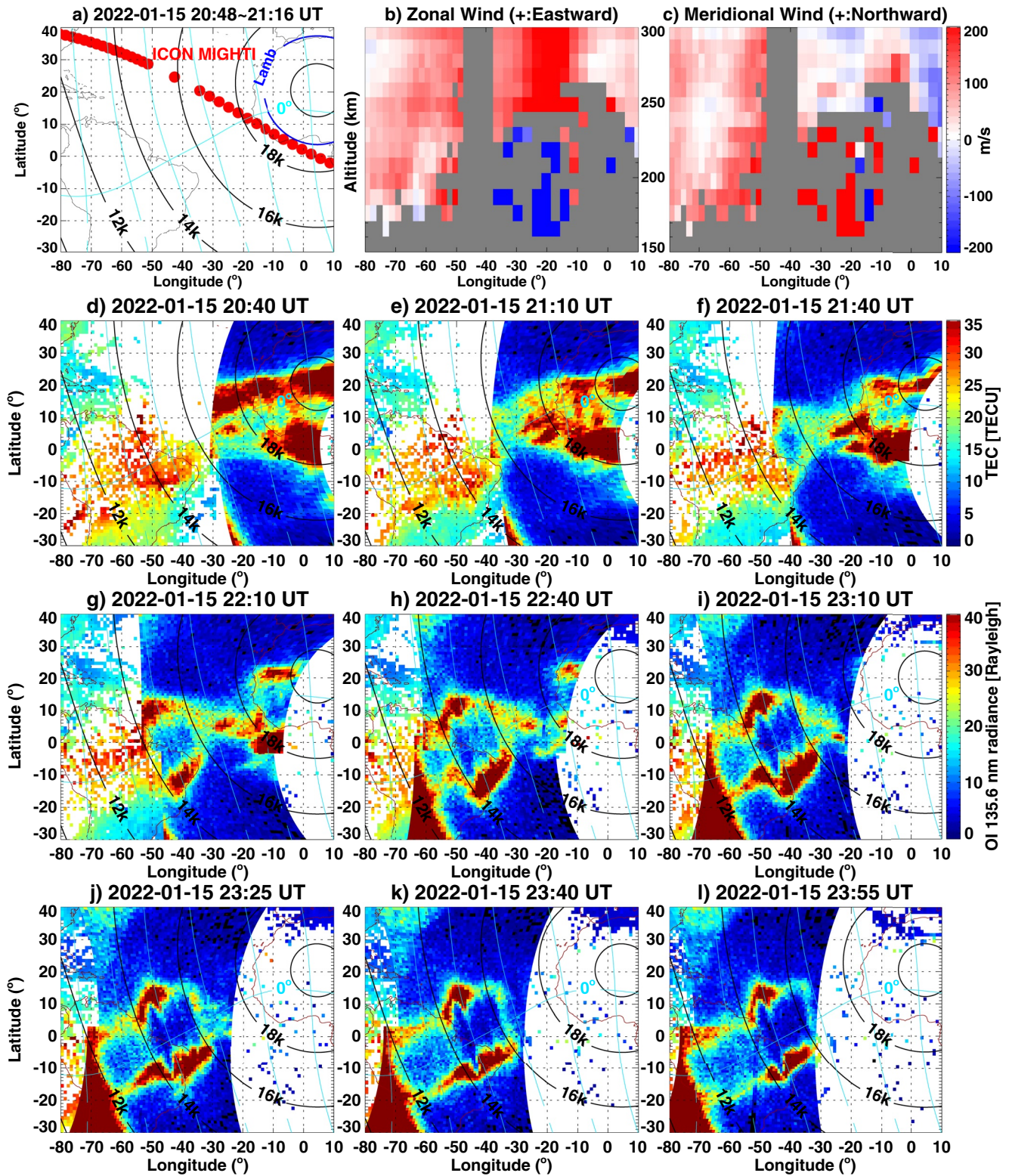


Figure 2. (a–c) Ionospheric Connection Explorer Michelson Interferometer for Global High-Resolution Thermospheric Imaging track and corresponding zonal wind and meridional wind profiles between 20:48–21:16 UT on 15 January 2022. The iso-distance circles away from the Tonga eruption epicenter are shown in black lines. The blue circle in Figure 2a is the estimated wavefront location of volcano-induced Lamb waves. (d–l) Combined Global Navigation Satellite System total electron content (TEC) and Global-scale Observations of the Limb and Disk OI 135.6-nm radiance maps in successive disk scan during 20:40–23:55 UT. The dip equator and meridional field lines are shown in cyan.

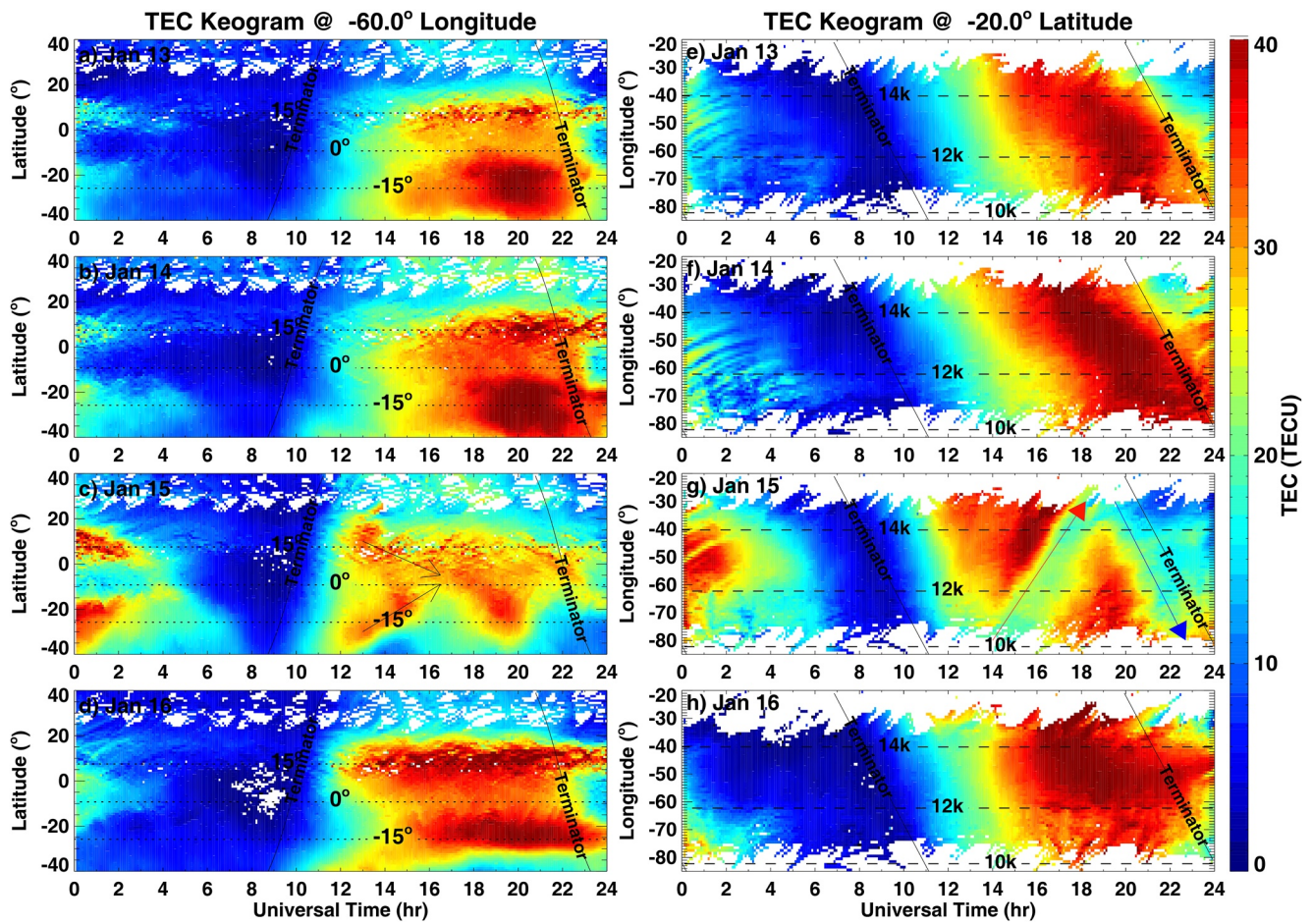


Figure 3. (a–d) Total electron content (TEC) keogram as a function of time and latitude along -60° longitude during Jan 13–16, respectively. The terminator (solid lines) and dip equator and $\pm 15^\circ$ geomagnetic latitudes are also marked. Two black arrows in Figure 3c mark the equatorward collapse of equatorial ionization anomaly crests. (e–h) TEC keogram as a function of time and longitude along -20° latitude during Jan 13–16, respectively. The iso-distance lines from volcano eruption are also shown. The red and blue arrows in Figure 3g mark two considerable TEC erosions.

30 and 60° W. However, at the trailing (right) side of the wave, EIA crest was significantly depleted by more than 10 TECU for two hours following the wave passage. The second EIA collapse (blue arrow) was observed during 21–24 UT near the dusk terminator with more than 10 TECU reduction, and was significantly different from the other 3 days with naturally prolonged evening EIA. This was likely related to the local sunset effect and the lower TEC background on January 15. Moreover, EIA suppression was associated with nighttime EPB inhibition between 00 and 06 UT in Figure 3h, in contrast to the other 3 days (Figures 3e–3g) which demonstrated clear EPBs signatures as dark streaks embedded in evening EIA crests. This suggests a weak or even reversed zonal electric field in the F region around X-pattern locations, driving a downward $E \times B$ drift and reducing the Rayleigh-Taylor instability via electrodynamic processes (Basu et al., 2009).

3.3. Wind and Plasma Drift Observations

Harding et al. (2022) reported ICON-MIGHTI wind measurements over two orbit passes and analyzed the dayside ionospheric dynamo response to the volcano eruption. Although Figures 2b and 2c have already shown dusktime wind measurements over a concentrated area, we extend this information by providing global wind measurements for six consecutive ICON-MIGHTI orbits in order to comprehensively investigate the possible prolonged dynamic and electrodynamic effects of volcano-induced waves. Figure 4 displays observation tracks and corresponding altitudinal profiles of thermospheric wind measurements across both E and F regions for six consecutive orbits on January 15. For the first two orbits between 13 and 16 UT, both zonal and meridional wind exhibited significant

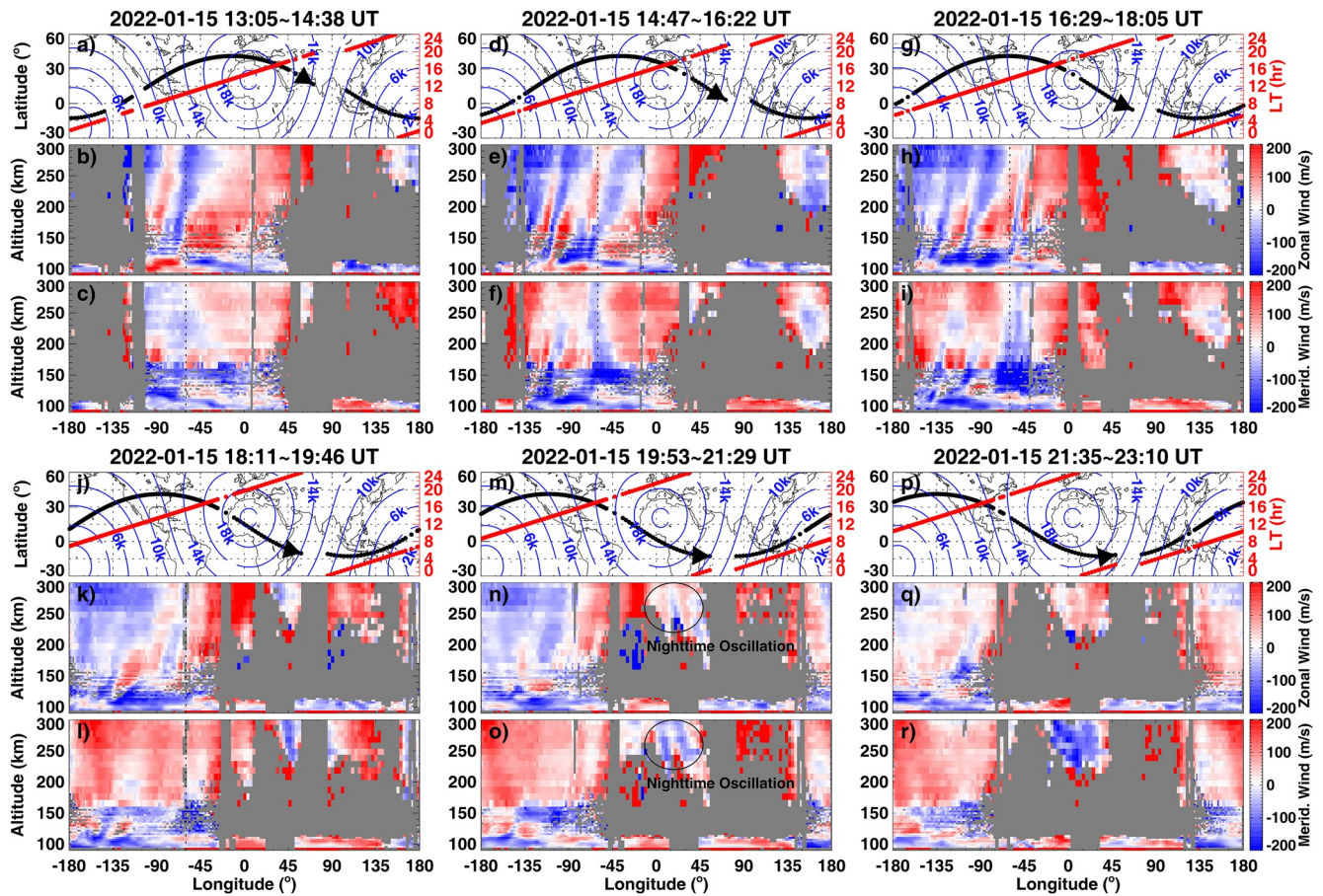


Figure 4. (a–r) Ionospheric Connection Explorer Michelson Interferometer for Global High-Resolution Thermospheric Imaging observation tracks and corresponding local time, zonal wind (positive eastward) and meridional wind (positive northward) profiles for six consecutive orbits on 15 January 2022. Iso-distance lines away from the Tonga volcano eruption epicenter with 2000 km interval are also marked on maps. The vertical dotted lines in wind profiles mark -60° longitude for comparison with total electron content keogram in Figure 3c. The ellipses in Figures 4n and 4o mark large nighttime F-region wind oscillations before Global-scale Observations of the Limb and Disk observed X-pattern signature.

quasi-periodic oscillations of ± 200 m/s over $30\text{--}100^\circ\text{W}$ longitudes around $9,000\text{--}14,000$ km from the volcano eruption epicenter. This was also reported in Harding et al. (2022) and agrees approximately with the timing of volcano-induced atmospheric Lamb waves as they swept across the American sector. The zonal wavelength was estimated to be $3,500\text{--}4,500$ km, assuming the wave does not change appreciably over the ~ 10 min required for the satellite to traverse one wave cycle. However, these wind fluctuations exhibited long-lasting perturbations that continued after the initial wavefront had already passed. The wind fluctuations were not only distinct in the orbit between $16:18\text{--}17:54$ UT, but also lasted at least $6\text{--}7$ hr in this longitudinal sector, since they can still be discerned around $21\text{--}22$ UT near 90°W in zonal wind results (Figures 4n and 4q). These long-lasting oscillations are consistent with those multiple-hour traveling ionospheric disturbance observations following the eruption induced Lamb waves (Zhang et al., 2022), partially demonstrating the notable energy from this volcano eruption comparing with other natural hazards or anthropogenic explosions (Jonah et al., 2021; Kundu et al., 2021).

To compare wind and TEC data, vertical dotted lines are drawn in wind profiles along 60°W longitude in a consistent manner with the TEC keogram in Figure 3c. At ~ 14 UT, zonal wind at this longitude has a sharp gradient from eastward to strongly westward of -150 m/s especially in the E region when the EIA crest in TEC started to exhibit depletion and collapse signatures. At ~ 16 UT, zonal wind near 60°W flipped from westward to eastward, associated with EIA crest depletion of more than 10 TECU and merging into a bright band at the equator. At $\sim 17:30$ UT, the zonal wind near 60°W exhibited large eastward components of $80\text{--}100$ m/s, and EIA crests were gradually enhanced and shifted poleward. At ~ 19 UT, the zonal wind near 60°W reversed back to slightly westward, and the intensity and position of EIA crests recovered to pre-depletion levels ~ 2 hr later. Thus,

the daytime EIA depletion can be explained by a westward equatorial electric field especially via the modified E region dynamo. These wind oscillations and EIA depletion-recovery results are in general agreement with a 1–2 hr thermosphere-ionosphere response delay, and build a robust connection between ionosphere EIA variations and thermosphere wind fluctuations. Moreover, the daytime meridional winds also have large perturbations that could partially modify the EIA intensity via dynamic and/or composition effect as mentioned in the introduction, which will be further described in the discussion part.

ICON MIGHTI nighttime wind observations also exhibited large horizontal wind oscillations in the F region with westward wind reversal. In particular, the longitudinal region between 15°W and 45°E in Figures 4n and 4o around 16,000–20,000 km away from volcano eruption show identifiable wavy signatures of wind oscillations (marked by ellipses) of ± 100 m/s around 21:20 UT. The location and time of these large-scale horizontal wind oscillations is generally consistent with GOLD measurements of X-pattern structure though with some data gaps, suggesting a wind causative effect with westward dynamo electric field that produced downward equatorial plasma drift and merged EIA crests. Despite the fact that the observed wind fluctuations are not exactly around the equatorial area due to MIGHTI's north-looking remote sensing geometry, it is reasonable to deduce that similar behavior should also occur in the equatorial region and the other hemisphere along the iso-distance lines via weakly-attenuated global-propagating Lamb waves (Nishida et al., 2014).

EIA perturbations existed also in the American sector ionosonde observations. Figure 5a shows electron density (N_e) profiles and F_2 region peak height (hmF2) as measured by the Fortaleza ionosonde (3.9°S, 38.4°W) during January 13–16, 2022. On January 15, hmF2 showed a drastic fluctuation that elevated up to 500 km at 15 UT followed by a very large decrease to 260 km at 17:30 UT. This behavior was not seen in other days in the same UT interval. hmF2 continued to experience large variations, increasing to 440 km at 21:30 UT and falling to 220 km at 00:30 UT on January 16. These wavelike hmF2 variations are consistent with the above-mentioned EIA fluctuation with two intervals of strong suppression. Figures 5b–5d show plasma drift results derived from Doppler measurements, with the shaded area marking the approximate passage time of Lamb waves. Results show that vertical drifts (Figure 5b) experienced a downward excursion of -15 m/s around 15 UT that contributed to the lowering of hmF2, followed by an upward enhancement of 30 m/s around 18 UT. Such a large drift reversal did not appear in other days at the same time, but was consistent with ICON zonal wind reversals as shown in Figures 4e and 4h. The eastward drift component on January 15 showed a large enhancement between 15 and 18 UT, reaching a maximum value of ~ 150 m/s that was notably larger than the other 3 days, and was likely caused by the dynamo action due to eruption-induced wind disturbances.

Figures 5e–5m display a sequence of Fortaleza ionograms showing the occurrence of spread-F with diffuse echoes in the F-layer traces between 21:50–23:10 UT on January 15. It is known that evening sector range-type equatorial spread-F is usually indicative of equatorial plasma bubbles produced at the bottomside F region by the Rayleigh-Taylor instability (Abdu, 2001; Woodman, 2009). However, the majority of these spread-F traces (Figures 5g–5m) should be classified as mixed-type or strong frequency-type spread-F, that is, the intensity of traces increases with frequency with no determinable critical frequencies (Cohen & Bowles, 1961). It indicates that irregularities were distributed in the whole F region, but the spreading was more severe near the F2-layer peak than in the bottomside part (Y. Chen et al., 2016). This usually means that ionospheric/thermospheric wave structures instead of localized PRE likely played a key role in triggering irregularities. Therefore, it was more likely that eruption-induced neutral wind oscillation and associated ion-neutral interaction led to the generation of polarization electric fields that seeded frequency-type spread-F (Tsunoda & Cosgrove, 2001). This further demonstrates the possible long-lasting effects of volcano-induced atmospheric waves and thermospheric-ionospheric perturbations that likely being the presupposition of observed X-pattern.

4. Discussion

As mentioned in the introduction, EIA variation is collectively determined by photo-chemistry, $E \times B$ drift, ambipolar diffusion, and neutral wind transportation. We next discuss the potential roles of lower atmospheric and/or geomagnetic forcing in modulating these terms to modify EIA crests in this event.

The daytime EIA in the American/Atlantic sector experienced drastic deformation between 14 and 17 UT on January 15 following the passage of volcano-induced Lamb waves. The crest intensity showed a slight enhancement in the leading side of the expected volcano-induced waves but a significant depletion of more than 10

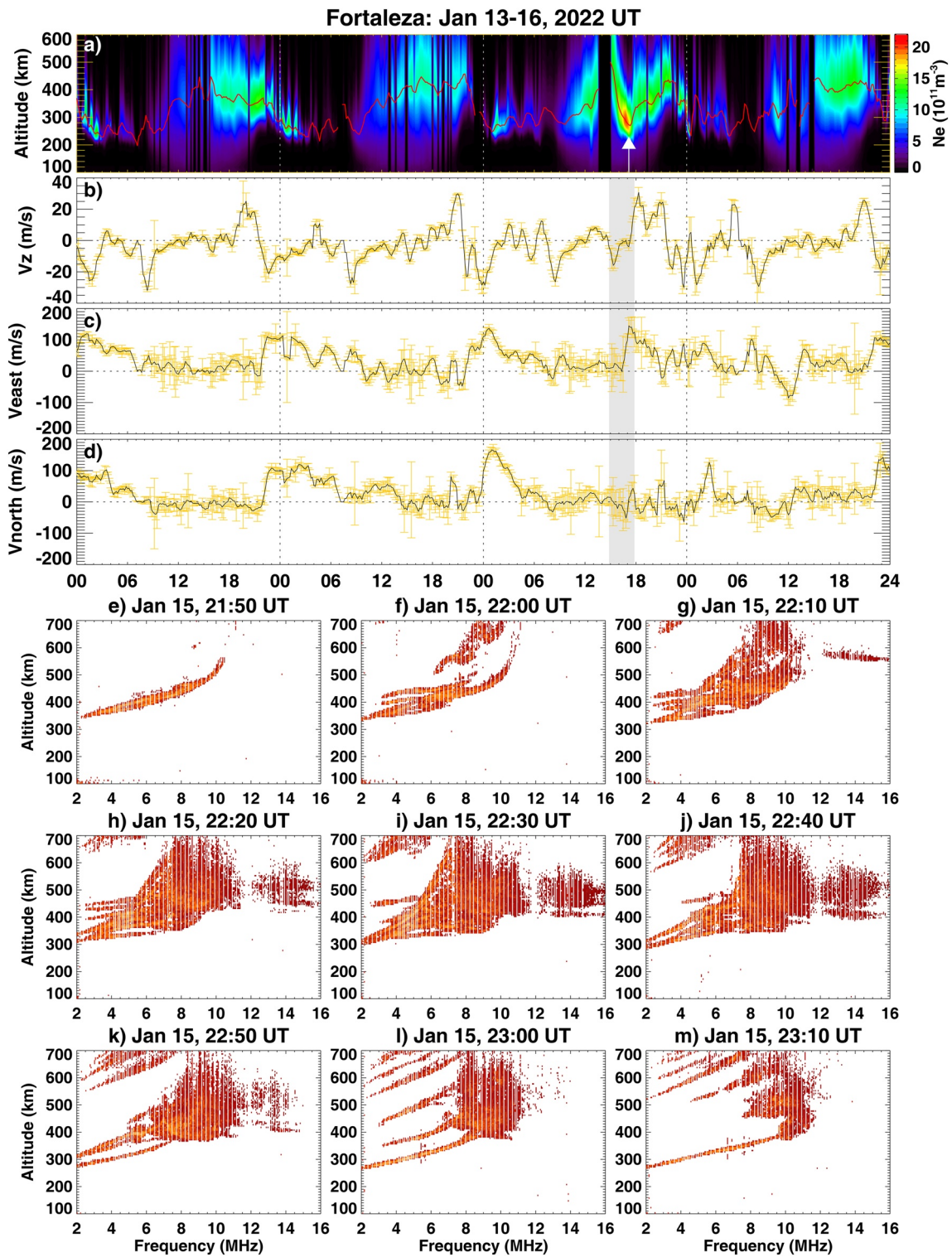


Figure 5. Fortaleza ionosonde measurements: (a) electron density profiles and F2-layer peak height (hmF2) during January 13–16, 2022. The white arrow marks significant hmF2 reduction. (b–d) Temporal variation of F layer vertical, eastward, and northward plasma drift with uncertainty error bars. The shaded area marks the approximate time periods when passage of volcano-induced Lamb waves and associated ionospheric disturbances occurred. (e–m) Sequence of ionograms showing the occurrence of spread-F during 21:50–23:10 UT on 15 January 2022.

TECU in the trailing side that continued for 2–3 hr. EIA crests almost merged together near the dip equator with no clear separation of two crests. This sudden EIA suppression and collapse has been occasionally reported and normally is attributed to suppression and/or reversal of the equatorial electrojet (EEJ) due to wind dynamo effects (e.g., Basu et al., 2009; Rastogi, 1974; Sreeja et al., 2009). In particular, Harding et al. (2022) reported that both Swarm A satellite data and ground-based magnetometers observed an eastward EEJ in the leading edge of the volcano-induced wavefront and a strong westward counter electrojet (CEJ) after the wave arrival. The ICON MIGHTI wind results therein and in our study also show strong oscillations, especially thermospheric zonal winds, that are in-phase with the appearance of EIA variation. In particular, the zonal wind oscillation at 60°W was consistent with the deformation and reformation of EIA crests with 1–2 hr response delay. Their correlation implies a plausible physics connection between thermosphere wind fluctuations and ionosphere EIA variation. Moreover, the Fortaleza ionosonde hmF2 also exhibited a considerable increase to 500 km at 15 UT then a dramatic decrease to 260 km at 17:30 UT following the downward vertical plasma drift. These dynamics again revealed that the directional change of zonal electric field leading to EIA suppression was associated with wind reversal during the passage of volcano-induced Lamb waves. The westward zonal wind reversal and associated neutral drag across the magnetic field lines is known to generate an upward polarization electric field via the E-region dynamo effect. Subsequently, the Hall current driven by this electric field further generates a westward electric field that can modulate equatorial zonal electric fields, producing downward equatorial plasma drift and observed EIA suppression (Heelis, 2004; Yamazaki et al., 2021).

The evening EIA in the American/Atlantic sector also experienced a dramatic deformation between 21 and 23 UT on January 15 with a unique X-pattern merging of EIA crests in GOLD ultraviolet images. This X-pattern was first captured during the Apollo 16 lunar mission in ultraviolet images of Earth's ionosphere (Carruthers & Page, 1972) and can be occasionally observed within GOLD OI 135.6 nm images during quiet times at longitudes where the geomagnetic equator crosses the geographic equator (Daniell et al., 2021). However, the underlying mechanisms of this X-pattern are still not known. The Tonga event provides natural experimental conditions to test our hypothesized electrodynamic effects on X-pattern formation, as this pattern occurred only on the eruption day while the preceding and following days showed more regular EIA morphology with clearly separated crests. The nightside X-pattern on January 15 appeared between a narrow longitudinal sector of 20–40°W, suggesting that the equatorial PRE through the F-region dynamo was likely reversed near the merging center. The ICON MIGHTI results in Figure 4 indicate that the longitudinally alternating reversal of F-region zonal wind has an approximate wavelength of ~3,500–4,500 km, consistent with the longitudinal span of the whole X-pattern (30–40°). In particular, Figures 2b and 4n showed noticeable wind oscillations in the F region with westward wind reversal around 21 UT after the estimated passage of volcano-induced Lamb waves, and EIA crests showed corresponding collapse in the following 1–2 hr with merging into a clear X-pattern near the largest wind gradient longitude area. In the F-region dynamo mechanism, strong zonal gradients in eastward winds and conductivity gradients near sunset can trigger strong downward polarization electric fields. These fields then produce considerable eastward electric fields as an edge effect due to the electric field curl-free requirement, and thus such eastward electric fields would drive PRE and maintain EIA crests (Eccles et al., 2015; J.; Chen & Lei, 2019; Rishbeth, 1971). Therefore, it is reasonable to suggest that the dramatic observed zonal wind oscillations with intense westward reversal reaching –200 m/s could lead to westward electric fields via an opposite dynamo action, driving a large downward plasma drift to substantially merge EIA crests in a central longitudinal sector and form observed evening X-pattern. This process can temporarily overtake the PRE effect.

The above eruption-induced electrodynamic processes through zonal wind oscillations provide a uniform scenario for EIA deformation in both daytime and nighttime. However, meridional wind dynamics, especially during concurrent geomagnetic disturbances, caused additional complications. In particular, Basu et al. (2009) indicated that an equatorward meridional wind can contribute to observed EIA collapse. ICON MIGHTI also observed considerable fluctuations in meridional winds between 14 and 18 UT over the American sector. It is theoretically possible that the volcano-induced equatorward wind perturbations, together with the storm-time equatorward wind surge, may have triggered neutral composition changes (O/N_2 depletion) to low-latitudes during the recovery phase, causing a negative ionospheric storm effect enhancing the EIA suppression. Considering the prevailing trans-equatorial wind from summer to winter hemisphere, this meridional wind effect may be more significant in the southern hemisphere, because TEC observations with larger EIA suppression occurred in the southern hemisphere. However, this potential effect requires future effort beyond the scope of this study.

In particular, verification of the effectiveness of this possible neutral dynamic contribution requires correct event timing as well as correct longitude location and proper disturbance intensity to reach specific EIA segments.

It is important to discuss whether the observed EIA deformation can be somewhat attributed to storm-time penetration and/or disturbance dynamo electric field effects. Figure 1b showed that IMF Bz exhibited a strong negative excursion followed by a quick northward turning at the end of January 14, indicating possible penetration electric field effects before the volcano eruption. Penetration effect is normally instant and short-lived lasting for ~hours. However, the observed daytime EIA suppression occurred 12 hr later after penetration effects would have subsided, and IMF Bz perturbation was limited between 04 and 15 UT on January 15. Thus, penetration electric field was unlikely the main cause of strong daytime EIA suppression. In contrast, the daytime EIA suppression (Figure 3g) appeared and propagated with a Lamb wave speed of 310–330 m/s, suggesting a more plausible connection with the volcano effect. On the other hand, the disturbance dynamo can lead to large equatorial downward drifts via westward wind perturbations, thereby causing a negative storm effect in the daytime (Fuller-Rowell et al., 1994; Sreeja et al., 2009). However, ICON MIGHTI observations do not completely agree with the presence of daytime disturbance dynamo effects. It is known the disturbance dynamo is a consequence of westward Coriolis forcing of equatorward neutral wind, and thus the disturbance wind is predominantly westward at low and mid-latitudes (Yamazaki & Maute, 2017). However, ICON/MIGHTI observed significant zonal wind oscillations with alternating eastward and westward wind perturbation within confined longitudinal bands of merely 15–20°. This is different from the westward feature of disturbance wind. Moreover, the magnitude of daytime disturbance wind is usually tens of meters at mid-latitudes (Xiong et al., 2015). However, both Harding et al. (2022) and the current study show that ICON/MIGHTI observed significant wind oscillations with westward reversals up to 200 m/s. These observed wind perturbations are different from and larger than the expected theoretical pattern of daytime disturbance dynamo. In addition, Le et al. (2022) have investigated EEJ and CEJ activities for this same event using the Swarm field-line current and ground-based magnetometer data, indicating that the penetration and disturbance dynamo electric field from this geomagnetic storm had minimal impact on the equatorial electric field perturbation.

During the presence of the evening X-pattern, IMF Bz fluctuated between ± 7 nT during 18–24 UT on January 15 due to the arrival of coronal hole high-speed streams, likely introducing intermittent penetration electric fields. However, the observed nightside EIA collapse and merging were confined in a narrow longitudinal area. It is thus hard to imagine that either the penetration or disturbance dynamo electric field would exhibit such a localized and oscillatory modulation.

5. Conclusions

The 2022 Tonga volcano eruption could have been a plausible source for the significant EIA deformation observed in the American sector about 12,000–16,000 km away from the epicenter, even 10+ hours after the eruption. This EIA variation was analyzed using GNSS TEC, GOLD ultraviolet measurements, ICON MIGHTI wind data, and ionosonde data. The main findings are as follows:

1. The daytime EIA especially the southern crest showed severe suppression of more than 10 TECU and collapsed equatorward for over 10° latitudes between 14 and 17 UT on January 15, following the passage of volcano-induced Lamb waves. This was associated with a downward equatorial plasma drift and drastic hmF2 reduction from 500 to 260 km as seen by the Forteleza ionosonde.
2. The nighttime EIA crests also experienced a similar suppression and equatorward shift around 21–23 UT, exhibiting a unique X-pattern in a limited longitudinal range of 20°–40°W. This was preceded by large horizontal wind oscillations including intense westward winds and was accompanied by strong frequency-type spread-F echoes in ionograms, plausibly representing prolonged thermosphere-ionosphere perturbations due to volcano-induced atmospheric waves.
3. Coincident with the daytime EIA suppression, thermospheric horizontal winds, especially zonal winds, exhibited significant quasi-periodic fluctuations between ± 200 m/s after the arrival of Volcano-induced Lamb waves in the American sector. These large zonal wind perturbations could significantly reverse the equatorial eastward zonal electric field primarily via the E-region dynamo effect, causing a strong downward plasma drift that led to daytime EIA suppression. The storm-related equatorward wind perturbations may have brought neutral composition changes to low-latitudes, partially modifying the EIA morphology.

- The estimated wavelength (~3,500–4,500 km) of zonal wind perturbations was consistent with the longitudinal scale size of the X-pattern (~30–40° longitudes). Prolonged horizontal wind modulations in the F region with strong westward reversal were observed preceding the evening X-pattern formation. This modulation with a strong westward wind gradient could trigger a large downward plasma drift that overturned PRE in a limited longitudinal area via F-region dynamo, leading to the observed evening X-pattern.

Data Availability Statement

Global Navigation Satellite System Total Electron Content data products are provided through the Madrigal distributed data system at (<http://cedar.openmadrigal.org/>) by MIT. The GOLD data can be accessed at (<https://gold.cs.ucf.edu/>). The Ionospheric Connection Explorer data can be accessed at (<https://icon.ssl.berkeley.edu/Data>). The solar wind and geophysical parameters data is acquired from NASA/GSFC's Space Physics Data Facility's OMNIWeb service (<https://cdaweb.gsfc.nasa.gov/>) and Kyoto world data center for Geomagnetism (<http://wdc.kugi.kyoto-u.ac.jp/>). The ionosonde data are provided by the University of Massachusetts Lowell DIDB database of Global Ionospheric Radio Observatory (<https://giro.uml.edu/didbase/scaled.php>).

References

- Aa, E., Zhang, S.-R., Erickson, P. J., Coster, A. J., Goncharenko, L. P., Varney, R. H., & Eastes, R. (2021). Salient Midlatitude Ionosphere-Thermosphere Disturbances Associated With SAPS During a Minor but Geo-Effective Storm at Deep Solar Minimum. *Journal of Geophysical Research: Space Physics*, *126*(7), e29509. <https://doi.org/10.1029/2021JA029509>
- Aa, E., Zou, S., Eastes, R., Karan, D. K., Zhang, S.-R., Erickson, P. J., & Coster, A. J. (2020). Coordinated ground-based and space-based observations of equatorial plasma bubbles. *Journal of Geophysical Research: Space Physics*, *125*(1), e27569. <https://doi.org/10.1029/2019JA027569>
- Abdu, M. A. (2001). Outstanding problems in the equatorial ionosphere-thermosphere electrodynamics relevant to spread F. *Journal of Atmospheric and Solar-Terrestrial Physics*, *63*(9), 869–884. [https://doi.org/10.1016/S1364-6826\(00\)00201-7](https://doi.org/10.1016/S1364-6826(00)00201-7)
- Anderson, D. N. (1973). A theoretical study of the ionospheric F region equatorial anomaly - I. Theory. *Planetary and Space Science*, *21*(3), 409–419. [https://doi.org/10.1016/0032-0633\(73\)90040-8](https://doi.org/10.1016/0032-0633(73)90040-8)
- Appleton, E. V. (1946). Two anomalies in the ionosphere. *Nature*, *157*(3995), 691. <https://doi.org/10.1038/157691a0>
- Balan, N., & Bailey, G. J. (1995). Equatorial plasma fountain and its effects: Possibility of an additional layer. *Journal of Geophysical Research*, *100*(A11), 21421–21432. <https://doi.org/10.1029/95JA01555>
- Balan, N., Liu, L., & Le, H. (2018). A brief review of equatorial ionization anomaly and ionospheric irregularities. *Earth and Planetary Physics*, *2*(4), 257–275. <https://doi.org/10.26464/epp2018025>
- Balan, N., Shiokawa, K., Otsuka, Y., Watanabe, S., & Bailey, G. J. (2009). Super plasma fountain and equatorial ionization anomaly during penetration electric field. *Journal of Geophysical Research*, *114*(A3), A03310. <https://doi.org/10.1029/2008JA013768>
- Basu, S., Basu, S., Huba, J., Krall, J., McDonald, S. E., Makela, J. J., et al. (2009). Day-to-day variability of the equatorial ionization anomaly and scintillations at dusk observed by GUVI and modeling by SAMI3. *Journal of Geophysical Research*, *114*(A4), A04302. <https://doi.org/10.1029/2008JA013899>
- Cai, X., Burns, A. G., Wang, W., Coster, A., Qian, L., Liu, J., et al. (2020). Comparison of GOLD nighttime measurements with total electron content: Preliminary results. *Journal of Geophysical Research: Space Physics*, *125*(9), e27767. <https://doi.org/10.1029/2019JA027767>
- Cai, X., Burns, A. G., Wang, W., Qian, L., Liu, J., Solomon, S. C., et al. (2021). Observation of postsunset OI 135.6 nm radiance enhancement over South America by the GOLD mission. *Journal of Geophysical Research: Space Physics*, *126*(2), e28108. <https://doi.org/10.1029/2020JA028108>
- Carruthers, G. R., & Page, T. (1972). Apollo 16 far-ultraviolet camera/spectrograph: Earth observations. *Science*, *177*(4051), 788–791. <https://doi.org/10.1126/science.177.4051.788>
- Chen, J., & Lei, J. (2019). A simulation study on the latitudinal variations of ionospheric zonal electric fields under geomagnetically quiet conditions. *Journal of Geophysical Research: Space Physics*, *124*(2), 1444–1453. <https://doi.org/10.1029/2018JA026174>
- Chen, Y., Liu, L., Le, H., Wan, W., & Zhang, H. (2016). Equatorial ionization anomaly in the low-latitude topside ionosphere: Local time evolution and longitudinal difference. *Journal of Geophysical Research: Space Physics*, *121*(7), 7166–7182. <https://doi.org/10.1002/2016JA022394>
- Cohen, R., & Bowles, K. L. (1961). On the nature of equatorial spread F. *Journal of Geophysical Research*, *66*(4), 1081–1106. <https://doi.org/10.1029/JZ066i004p1081>
- Dang, T., Luan, X., Lei, J., Dou, X., & Wan, W. (2016). A numerical study of the interhemispheric asymmetry of the equatorial ionization anomaly in solstice at solar minimum. *Journal of Geophysical Research: Space Physics*, *121*(9), 9099–9110. <https://doi.org/10.1002/2016JA023012>
- Daniell, R. E., Karan, D. K., Martinis, C. R., & Eastes, R. (2021). The Occurrence of X-Patterns in the Nighttime Equatorial Ionization Anomaly (EIA) Observed in 135.6 nm Images from the Global-scale Observations of Limb and Disk (GOLD) Mission. In *AGU Fall Meeting Abstracts* (Vol. 2021). SA51A-07.
- Das, A., Paul, K. S., Halder, S., Basu, K., & Paul, A. (2014). Characteristics of equatorial ionization anomaly (EIA) in relation to transionospheric satellite links around the northern crest in the Indian longitude sector. *Annales Geophysicae*, *32*(2), 91–97. <https://doi.org/10.5194/angeo-32-91-2014>
- Duncan, R. A. (1960). The equatorial F-region of the ionosphere. *Journal of Atmospheric and Terrestrial Physics*, *18*(2), 89–100. [https://doi.org/10.1016/0021-9169\(60\)90081-7](https://doi.org/10.1016/0021-9169(60)90081-7)
- Eastes, R. W., McClintock, W. E., Burns, A. G., Anderson, D. N., Andersson, L., Aryal, S., et al. (2020). Initial observations by the GOLD mission. *Journal of Geophysical Research: Space Physics*, *125*(7), e27823. <https://doi.org/10.1029/2020JA027823>
- Eastes, R. W., McClintock, W. E., Burns, A. G., Anderson, D. N., Andersson, L., Codrescu, M., et al. (2017). The Global-scale Observations of the Limb and Disk (GOLD) mission. *Space Science Reviews*, *212*(1–2), 383–408. <https://doi.org/10.1007/s11214-017-0392-2>
- Eastes, R. W., Solomon, S. C., Daniell, R. E., Anderson, D. N., Burns, A. G., England, S. L., et al. (2019). Global-scale observations of the equatorial ionization anomaly. *Geophysical Research Letters*, *46*(16), 9318–9326. <https://doi.org/10.1029/2019GL084199>

Acknowledgments

Global Navigation Satellite System Total Electron Content data are generated as part of the Millstone Hill Geospace Facility program, operated by the Massachusetts Institute of Technology (MIT) under NSF AGS-1952737. We acknowledge NSF awards AGS-2033787, AGS-2033843, and PHY-2028125, NASA support 80NSSC22K0171, 80NSSC21K1310, 80NSSC21K1775, 80NSSC19K0834, 80NSSC17K0013, 80NSSC19K0835, 80NSSC20K0601, and 80NSSC20K0356, AFOSR MURI Project FA9559-16-1-0364, and ONR Grant N00014-17-1-2186. Data for TEC processing is provided from the following organizations: UNAVCO, SOPAC, IGN (France), IGS, CDDIS, NGS, IBGE (Brazil), RAMSAC (Argentina), CORS (Panama), Arecibo Observatory, LISN, Topcon, CHAIN (Canada), CRS (Italy), SONEI, RENAG (New Zealand), GNSS Reference Networks, Finnish Meteorological Institute, and SWEPOS. National Center for Atmospheric Research is sponsored by the National Science Foundation.

- Eccles, J. V., St Maurice, J. P., & Schunk, R. W. (2015). Mechanisms underlying the prereversal enhancement of the vertical plasma drift in the low-latitude ionosphere. *Journal of Geophysical Research: Space Physics*, *120*(6), 4950–4970. <https://doi.org/10.1002/2014JA020664>
- Englert, C. R., Harlander, J. M., Brown, C. M., Marr, K. D., Miller, I. J., Stump, J. E., et al. (2017). Michelson interferometer for global high-resolution thermospheric imaging (MIGHTI): Instrument design and calibration. *Space Science Reviews*, *212*(1–2), 553–584. <https://doi.org/10.1007/s11214-017-0358-4>
- Fang, T.-W., Fuller-Rowell, T., Yudin, V., Matsuo, T., & Viereck, R. (2018). Quantifying the sources of ionosphere day-to-day variability. *Journal of Geophysical Research: Space Physics*, *123*(11), 9682–9696. <https://doi.org/10.1029/2018JA025525>
- Farley, D. T., Bonelli, E., Fejer, B. G., & Larsen, M. F. (1986). The prereversal enhancement of the zonal electric field in the equatorial ionosphere. *Journal of Geophysical Research*, *91*(A12), 13723–13728. <https://doi.org/10.1029/JA091iA12p13723>
- Fuller-Rowell, T. J., Codrescu, M. V., Moffett, R. J., & Quegan, S. (1994). Response of the thermosphere and ionosphere to geomagnetic storms. *Journal of Geophysical Research*, *99*(A3), 3893–3914. <https://doi.org/10.1029/93JA02015>
- Gan, Q., Eastes, R. W., Burns, A. G., Wang, W., Qian, L., Solomon, S. C., et al. (2020). New observations of large-scale waves coupling with the ionosphere made by the GOLD mission: Quasi-16-day wave signatures in the F-region OI 135.6-nm nightglow during sudden stratospheric warmings. *Journal of Geophysical Research: Space Physics*, *125*(4), e27880. <https://doi.org/10.1029/2020JA027880>
- Goncharenko, L. P., Chau, J. L., Liu, H. L., & Coster, A. J. (2010). Unexpected connections between the stratosphere and ionosphere. *Geophysical Research Letters*, *37*(10), L10101. <https://doi.org/10.1029/2010GL043125>
- Hanson, W. B., & Moffett, R. J. (1966). Ionization transport effects in the equatorial F region. *Journal of Geophysical Research*, *71*(23), 5559–5572. <https://doi.org/10.1029/JZ071i023p05559>
- Harding, B. J., Makela, J. J., Englert, C. R., Marr, K. D., Harlander, J. M., England, S. L., & Immel, T. J. (2017). The MIGHTI wind retrieval algorithm: Description and verification. *Space Science Reviews*, *212*(1–2), 585–600. <https://doi.org/10.1007/s11214-017-0359-3>
- Harding, B. J., Wu, Y.-J. J., Alken, P., Yamazaki, Y., Triplett, C. C., Immel, T. J., et al. (2022). Impacts of the January 2022 Tonga volcanic eruption on the ionospheric dynamo: ICON-MIGHTI and Swarm observations of extreme neutral winds and currents. *Geophysical Research Letters*, *49*(9), e2022GL098577. <https://doi.org/10.1029/2022GL098577>
- Heelis, R. A. (2004). Electrodynamics in the low and middle latitude ionosphere: A tutorial. *Journal of Atmospheric and Solar-Terrestrial Physics*, *66*(10), 825–838. <https://doi.org/10.1016/j.jastp.2004.01.034>
- Huang, H., Lu, X., Liu, L., Wang, W., & Li, Q. (2018). Transition of interhemispheric asymmetry of equatorial ionization anomaly during solstices. *Journal of Geophysical Research: Space Physics*, *123*(12), 10283–10300. <https://doi.org/10.1029/2018JA026055>
- Immel, T. J., England, S. L., Mende, S. B., Heelis, R. A., Englert, C. R., Edelstein, J., et al. (2018). The ionospheric connection explorer mission: Mission goals and design. *Space Science Reviews*, *214*(1), 13. <https://doi.org/10.1007/s11214-017-0449-2>
- Immel, T. J., Sagawa, E., England, S. L., Henderson, S. B., Hagan, M. E., Mende, S. B., et al. (2006). Control of equatorial ionospheric morphology by atmospheric tides. *Geophysical Research Letters*, *33*(15), L15108. <https://doi.org/10.1029/2006GL026161>
- Jayachandran, P. T., Sri Ram, P., Somayajulu, V. V., & Rama Rao, P. V. S. (1997). Effect of equatorial ionization anomaly on the occurrence of spread-F. *Annales Geophysicae*, *15*(2), 255–262. <https://doi.org/10.1007/s00585-997-0255-3>
- Jonah, O. F., Vergados, P., Krishnamoorthy, S., & Komjathy, A. (2021). Investigating ionospheric perturbations following the 2020 Beirut explosion event. *Radio Science*, *56*(10), e07302. <https://doi.org/10.1029/2021RS007302>
- Karan, D. K., Daniell, R. E., England, S. L., Martinis, C. R., Eastes, R. W., Burns, A. G., & McClintock, W. E. (2020). First zonal drift velocity measurement of Equatorial Plasma Bubbles (EPBs) from a geostationary orbit using GOLD data. *Journal of Geophysical Research: Space Physics*, *125*(9), e28173. <https://doi.org/10.1029/2020JA028173>
- Khadka, S. M., Valladares, C. E., Sheehan, R., & Gerrard, A. J. (2018). Effects of electric field and neutral wind on the asymmetry of equatorial ionization anomaly. *Radio Science*, *53*(5), 683–697. <https://doi.org/10.1029/2017RS006428>
- Kil, H., Demajistre, R., Paxton, L. J., & Zhang, Y. (2006). Nighttime F-region morphology in the low and middle latitudes seen from DMSF F15 and TIMED/GUVI. *Journal of Atmospheric and Solar-Terrestrial Physics*, *68*(14), 1672–1681. <https://doi.org/10.1016/j.jastp.2006.05.024>
- Kundu, B., Senapati, B., Matsushita, A., & Heki, K. (2021). Atmospheric wave energy of the 2020 August 4 explosion in Beirut, Lebanon, from ionospheric disturbances. *Scientific Reports*, *11*(1), 2793. <https://doi.org/10.1038/s41598-021-82355-5>
- Le, G., Liu, G., Yizengaw, E., & Englert, C. (2022). Intense Equatorial Electrojet and Counter Electrojet caused by the 15 January 2022 Tonga Volcanic Eruption: Space and Ground-based Observations. *Earth and Space Science Open Archive*. <https://doi.org/10.1002/essoar.10511040.2>
- Lei, J., Thayer, J. P., Wang, W., Luan, X., Dou, X., & Roble, R. (2012). Simulations of the equatorial thermosphere anomaly: Physical mechanisms for crest formation. *Journal of Geophysical Research*, *117*(A6), A06318. <https://doi.org/10.1029/2012JA017613>
- Lin, C. H., Liu, J. Y., Fang, T. W., Chang, P. Y., Tsai, H. F., Chen, C. H., & Hsiao, C. C. (2007). Motions of the equatorial ionization anomaly crests imaged by FORMOSAT-3/COSMIC. *Geophysical Research Letters*, *34*(19), L19101. <https://doi.org/10.1029/2007GL030741>
- Liu, H.-L. (2020). Day-to-day variability of prereversal enhancement in the vertical ion drift in response to large-scale forcing from the lower atmosphere. *Space Weather*, *18*(4), e02334. <https://doi.org/10.1029/2019SW002334>
- Luan, X., Wang, P., Dou, X., & Liu, Y. C. M. (2015). Interhemispheric asymmetry of the equatorial ionization anomaly in solstices observed by COSMIC during 2007–2012. *Journal of Geophysical Research: Space Physics*, *120*(4), 3059–3073. <https://doi.org/10.1002/2014JA020820>
- Makela, J. J., Baughman, M., Navarro, L. A., Harding, B. J., Englert, C. R., Harlander, J. M., et al. (2021). Validation of ICON MIGHTI Thermospheric Wind Observations: 1. Nighttime Red Line Ground Based Fabry Perot Interferometers. *Journal of Geophysical Research: Space Physics*, *126*(2), e28726. <https://doi.org/10.1029/2020JA028726>
- Nishida, K., Kobayashi, N., & Fukao, Y. (2014). Background Lamb waves in the Earth's atmosphere. *Geophysical Journal International*, *196*(1), 312–316. <https://doi.org/10.1093/gji/ggt413>
- Paul, A., & Dasgupta, A. (2010). Characteristics of the equatorial ionization anomaly in relation to the day-to-day variability of ionospheric irregularities around the postsunset period. *Radio Science*, *45*(6), RS6001. <https://doi.org/10.1029/2009RS004329>
- Rastogi, R. G. (1974). Westward equatorial electrojet during daytime hours. *Journal of Geophysical Research*, *79*(10), 1503–1512. <https://doi.org/10.1029/JA079i010p01503>
- Rideout, W., & Coster, A. (2006). Automated GPS processing for global total electron content data. *GPS Solutions*, *10*(3), 219–228. <https://doi.org/10.1007/s10291-006-0029-5>
- Rishbeth, H. (1971). The F-layer dynamo. *Planetary and Space Science*, *19*(2), 263–267. [https://doi.org/10.1016/0032-0633\(71\)90205-4](https://doi.org/10.1016/0032-0633(71)90205-4)
- Sreeja, V., Ravindran, S., Pant, T. K., Devasia, C. V., & Paxton, L. J. (2009). Equatorial and low-latitude ionosphere-thermosphere system response to the space weather event of August 2005. *Journal of Geophysical Research*, *114*(A12), A12307. <https://doi.org/10.1029/2009JA014491>
- Su, Y. Z., Bailey, G. J., Oyama, K. I., & Balan, N. (1997). A modelling study of the longitudinal variations in the north-south asymmetries of the ionospheric equatorial anomaly. *Journal of Atmospheric and Solar-Terrestrial Physics*, *59*(11), 1299–1310. [https://doi.org/10.1016/S1364-6826\(96\)00016-8](https://doi.org/10.1016/S1364-6826(96)00016-8)

- Themens, D. R., Watson, C., Žagar, N., Vasylykevych, S., Elvidge, S., McCaffrey, A., et al. (2022). Global propagation of ionospheric disturbances associated with the 2022 Tonga Volcanic Eruption. *Geophysical Research Letters*, *49*(7), e98158. <https://doi.org/10.1029/2022GL098158>
- Thomas, L. (1968). The F2-region equatorial anomaly during solstice periods at sunspot maximum. *Journal of Atmospheric and Terrestrial Physics*, *30*(9), 1631–1640. [https://doi.org/10.1016/0021-9169\(68\)90011-1](https://doi.org/10.1016/0021-9169(68)90011-1)
- Tsunoda, R. T., & Cosgrove, R. B. (2001). Coupled electrodynamics in the nighttime midlatitude ionosphere. *Geophysical Research Letters*, *28*(22), 4171–4174. <https://doi.org/10.1029/2001GL013245>
- Tsurutani, B., Mannucci, A., Iijima, B., Abdu, M. A., Sobral, J. H. A., Gonzalez, W., & Vasyliunas, V. M. (2004). Global dayside ionospheric uplift and enhancement associated with interplanetary electric fields. *Journal of Geophysical Research*, *109*(A8), A08302. <https://doi.org/10.1029/2003JA010342>
- Tulasi Ram, S., Su, S. Y., & Liu, C. H. (2009). FORMOSAT-3/COSMIC observations of seasonal and longitudinal variations of equatorial ionization anomaly and its interhemispheric asymmetry during the solar minimum period. *Journal of Geophysical Research*, *114*(A6), A06311. <https://doi.org/10.1029/2008JA013880>
- Vierinen, J., Coster, A. J., Rideout, W. C., Erickson, P. J., & Norberg, J. (2016). Statistical framework for estimating GNSS bias. *Atmospheric Measurement Techniques*, *9*(3), 1303–1312. <https://doi.org/10.5194/amt-9-1303-2016>
- Wan, X., Zhong, J., Xiong, C., Wang, H., Liu, Y., Li, Q., et al. (2021). Seasonal and Interhemispheric Effects on the Diurnal Evolution of EIA: Assessed by IGS TEC and IRI-2016 over Peruvian and Indian Sectors. *Remote Sensing*, *14*(1), 107. <https://doi.org/10.3390/rs14010107>
- Woodman, R. F. (2009). Spread F - An old equatorial aeronomy problem finally resolved? *Annales Geophysicae*, *27*(5), 1915–1934. <https://doi.org/10.5194/angeo-27-1915-2009>
- Xiong, C., Lühr, H., & Fejer, B. G. (2015). Global features of the disturbance winds during storm time deduced from CHAMP observations. *Journal of Geophysical Research: Space Physics*, *120*(6), 5137–5150. <https://doi.org/10.1002/2015JA021302>
- Xiong, C., Lühr, H., & Ma, S. (2013). The magnitude and inter-hemispheric asymmetry of equatorial ionization anomaly-based on champ and grace observations. *Journal of Atmospheric and Solar-Terrestrial Physics*, *105–106*, 160–169. <https://doi.org/10.1016/j.jastp.2013.09.010>
- Yamazaki, Y. (2018). Quasi-6-day wave effects on the equatorial ionization anomaly over a solar cycle. *Journal of Geophysical Research: Space Physics*, *123*(11), 9881–9892. <https://doi.org/10.1029/2018JA026014>
- Yamazaki, Y., Harding, B. J., Stolle, C., & Matzka, J. (2021). Neutral wind profiles during periods of eastward and westward equatorial electrojet. *Geophysical Research Letters*, *48*(11), e93567. <https://doi.org/10.1029/2021GL093567>
- Yamazaki, Y., & Maute, A. (2017). Sq and EEJ—A review on the daily variation of the geomagnetic field caused by ionospheric dynamo currents. *Space Science Reviews*, *206*(1–4), 299–405. <https://doi.org/10.1007/s11214-016-0282-z>
- Zhang, S.-R., Vierinen, J., Aa, E., Goncharenko, L. P., Erickson, P. J., Rideout, W., et al. (2022). 2022 Tonga volcanic eruption induced global propagation of ionospheric disturbances via lamb waves. *Frontiers in Astronomy and Space Sciences*, *9*, 871275. <https://doi.org/10.3389/fspas.2022.871275>
- Zhao, B., Wan, W., Liu, L., & Ren, Z. (2009). Characteristics of the ionospheric total electron content of the equatorial ionization anomaly in the Asian-Australian region during 1996–2004. *Annales Geophysicae*, *27*(10), 3861–3873. <https://doi.org/10.5194/angeo-27-3861-2009>